ACS APPLIED MATERIALS & INTERFACES

www.acsami.org

Research Article

Flash Joule Heating Synthesis of Layer-Stacked Vanadium Oxide/Graphene Hybrids within Seconds for High-Performance Aqueous Zinc-Ion Batteries

Xiaoxin Lv, Aomen Yang, Menglian Wang, Kaiqi Nie, Jiujun Deng,* and Xuhui Sun*

Cite This: https://doi.org/10.1021/acsami.4c10376

Read Online

ACCESS | Metrics & More | Article Recommendations | Supporting Information

ABSTRACT: Vanadium oxides have been regarded as highly promising cathodes for aqueous zinc-ion batteries (ZIBs). However, obtaining high-performance vanadium oxide-based cathodes suitable for industrial application remains a significant challenge due to the need for cost-effective, straightforward, and efficient preparation methods. Herein, we present a facile and rapid synthesis of a composite cathode, consisting of layer-stacked VO_2/V_2O_5 and graphene-like carbon nanosheets, in just 2.5 s by treating the commercial V_2O_5 powder via a flash Joule heating strategy. When employed as the cathode for ZIBs, the resulting composite delivers a comparable rate capacity of 459 mA h g^{-1} at 0.2 A g^{-1} and remarkable cycle stabilities of 355.5 mA h g^{-1} after 2500 cycles at 1.0 A g^{-1} and 169.5 mA h g^{-1} after 10,000 cycles at 10 A g^{-1}, respectively. Further electrochemical analysis reveals that the impressive performance is attributed to the accelerated charge transfer and the alleviated structure degradation, facilitated by the abundant sites and a built-in electric field of the layer-stacked VO_2/V_2O_5 heterostructure, as well as the excellent conductivity of graphene-like carbon nanosheets. This work introduces a unique approach for ultrafast and low-cost fabrication of high-performance vanadium oxide-based composite cathodes toward efficient ZIBs.

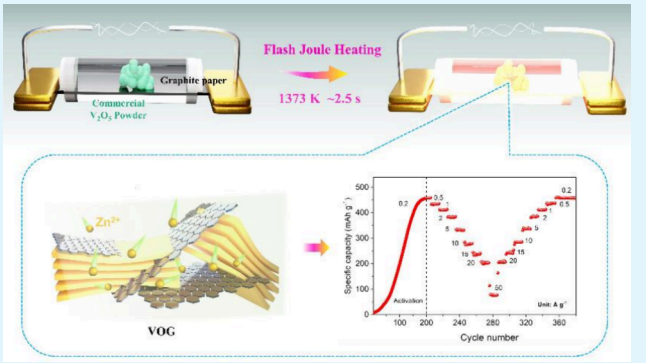

KEYWORDS: *vanadium oxide, zinc-ion batteries, cathode, graphene, Joule heating*

INTRODUCTION

Nowadays, lithium-ion batteries (LIBs) are widely used in electric vehicles and portable electronic devices because of their high energy density and impressive cycling stability.[1−4] However, limited lithium resources and safety issues significantly hinder the future development of LIBs. Recently, alternative devices such as sodium-ion batteries (SIBs),[2,3] potassium-ion batteries (KIBs),[4] and zinc-ion batteries (ZIBs)[5−8] have emerged as promising candidates for next-generation energy storage systems. In particular, aqueous ZIBs have shown greater potential due to the notable merits of the zinc metal such as low redox potential (−0.76 V versus the standard hydrogen electrode), ultrahigh theoretical capacity (820 mA h g^{-1}), abundant resources, high safety, and low cost.[5−8] Recent advancements have focused on developing high-performance cathodes for efficient ZIBs, and a wide range of materials such as manganese compounds,[9,10] Prussian blue analogs,[11] organic polymers,[12] and vanadium-based oxides[13−16] have been exploited. Among the materials, vanadium oxides including V_2O_5, VO_2, and V_2O_3 have demonstrated significant promise owing to their high revisable capacities and prominent rate performance resulting from the multitudinous crystal structures and valence states.[13−16] Nevertheless, the practical application of the vanadium oxide cathode is still strictly limited by intrinsic drawbacks, for example, the sluggish Zn^{2+}/electron transfer kinetics originated from the low electrical conductivity and the poor stability caused by the severe structural degradation during cycling.[13−16]

To address these issues, diverse strategies such as designing materials in nanoscale size, incorporating metal ions, and constructing composites have been developed to significantly enhance the electrochemical performance of vanadium oxides.[13−22] Therein, the fabrication of layered vanadium oxide cathodes has shown notable advantages since the two-dimensional structure could facilitate the penetration of the electrolyte solution and accommodate the volume change during the charge and discharge processes by providing abundant active sites and increasing the contact area.[18,19] Likewise, integrating vanadium oxides with nanocarbon (e.g., graphene, carbon nanotube, and porous carbon) has also

Received: June 23, 2024
Revised: September 5, 2024
Accepted: September 9, 2024

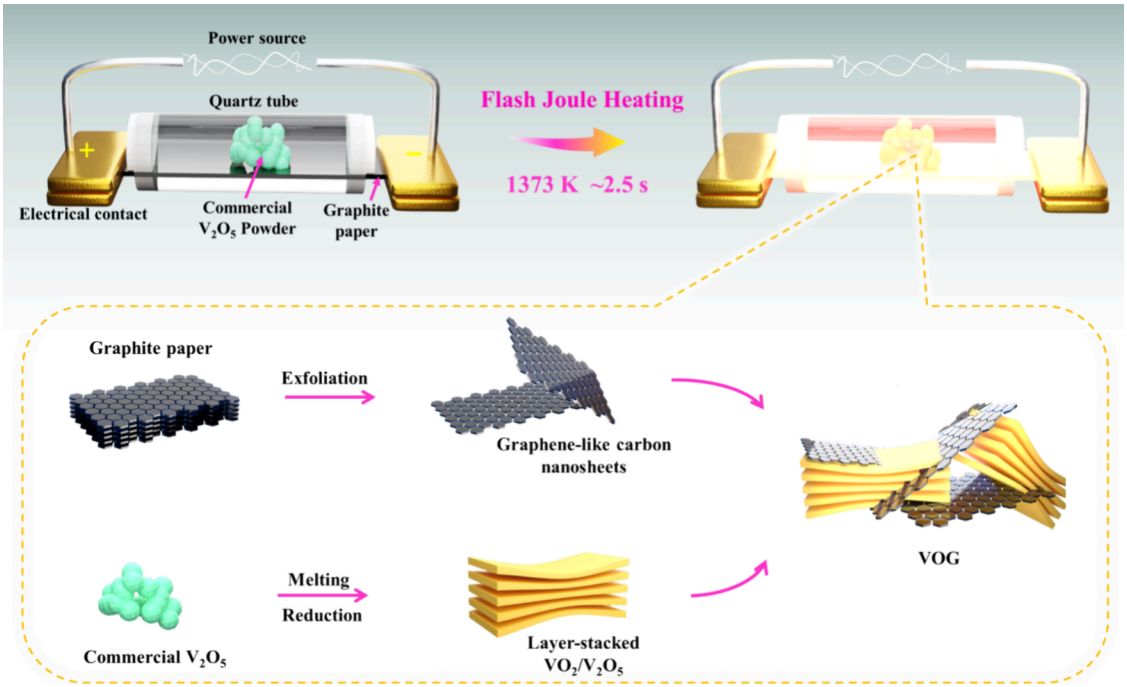

Figure 1. Schematic illustration for the fabrication of the VOG composite.

proven effective in facilitating Zn^{2+}/electron transport and maintaining structural stability, benefiting from the excellent electrical conductivity and the high chemical stability of nanocarbon.[20−22] However, obtaining efficient layered/nanocarbon vanadium oxide composite cathodes suitable for industrial application via a low-cost and facile method remains a challenge. Most of those cathodes are synthesized through a procedure with high-energy consumption, multiple steps, long production time, and pollutant production, which severely limits the further development of aqueous ZIBs.[23]

Compared to conventional heating processes, the ultrahigh temperature and the ultrafast heating/quenching rates (over the order of 10^5 K s^{-1}) of flash Joule heating (FJH) enable the synthesis of functional materials more facile, affordable, and effective by simplifying the tedious heating steps and reducing the energy consumption.[23−25] In such an end, the FJH technique as a promising synthesis strategy has been widely utilized to create novel nanomaterials.[26−30] For example, Luong et al. demonstrated that the FJH of inexpensive carbon sources could afford gram-scale quantities of graphene in less than one second.[27] More recently, Li et al. reported the ultrafast and in situ synthesis of transition metal-layered hydroxides on carbon cloth substrates within a dozen seconds via a FJH method in the metal salt solution, and the as-prepared sample exhibited an excellent electrochemical performance when used as a cathode for ZIBs.[23]

In this work, we demonstrate a facile and ultrafast fabrication of a composite cathode consisting of layer-stacked VO_2/V_2O_5 microstructures and graphene-like carbon nanosheets (labeled as VOG) within 2.5 s by treating the commercial V_2O_5 powder through the FJH procedure. In this process, the instantaneous high-temperature heating and quenching of FJH provide sufficient energy to convert the commercial V_2O_5 powder into layer-stacked VO_2/V_2O_5 microstructures via melting, reduction, and aggregation. At the same time, the melting of the V_2O_5 powder etches the surface of the underlying graphite paper substrate to introduce graphene-like carbon nanosheets into the composite. Upon use as the cathode for aqueous ZIBs, the as-resulted VOG composite delivers a rate capacity of 459 mA h g^{-1} at 0.2 A g^{-1} and remarkable cycle stabilities in both high and low current densities (355.5 mA h g^{-1} after 2500 cycles at 1.0 A g^{-1} and 169.5 mA h g^{-1} after 10,000 cycles at 10 A g^{-1}) by accelerating the electron/Zn ion transfer and alleviating the structure degradation owing to abundant storage sites and a built-in electric field of the layer-stacked VO_2/V_2O_5 heterostructure, as well as the excellent electric conductivity of graphene-like carbon nanosheets. This work opens a facile and efficient approach for obtaining high-performance vanadium oxide-based cathodes toward efficient ZIBs.

RESULTS AND DISCUSSION

Figure 1 illustrates the experimental setup and preparation processes of the VOG composite based on the FJH technique. In a typical FJH procedure, a high temperature above 1300 K could be produced within a very short time of ~2.5 s (a heating speed of ~550 K s^{-1}) by applying a current pulse on the conductive graphite paper substrate, as demonstrated in Figure S1. In such a case, the carbothermal shock would enable the commercial V_2O_5 powder to melt, aggregate, and reduce into the layer-stacked VO_2/V_2O_5 microstructure due to the low melting point (~681 °C) and the lamellar or layered crystal structure of V_2O_5,[31] as described by the following equation:

$$V_2O_5\ (\text{partial}) + C \xrightarrow{\Delta} VO_2 + CO_2\uparrow \quad (1)$$

Concomitantly, the melting of V_2O_5 powder would detach graphene-like carbon nanosheets from the underlying graphite paper substrate (Figure S2) into the as-resulted samples. Eventually, a composite composed of graphene-like carbon nanosheets and a layer-stacked VO_2/V_2O_5 block were constructed, as unraveled by scanning electron microscope (SEM) images and energy dispersive spectroscopy (EDS) mappings in Figure 2a−e. It is further confirmed by

https://doi.org/10.1021/acsami.4c10376
ACS Appl. Mater. Interfaces XXXX, XXX, XXX−XXX

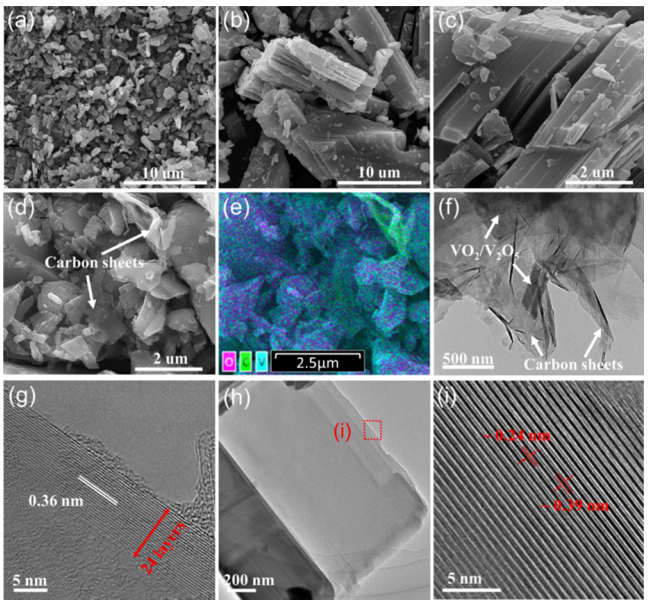

Figure 2. SEM images of commercial V_2O_5 (a) and VOG composite (b–d); energy dispersive spectroscopy (EDS) mapping (e), and HRTEM images (f–i) of the VOG composite.

transmission electron microscope (TEM) characterizations. As shown in Figure 2f,h, the low-magnification TEM images reveal the layered structure of VO_2/V_2O_5 and graphene-like carbon nanosheets in the VOG composite. The high-resolution TEM (HRTEM) image in Figure 2g further shows that the layer spacing of 0.36 nm of multilayered carbon sheets (the thicknesses are in the range of 4–24 layers, depending on the location) is consistent with that of graphene in the literature.[32,33] For the VO_2/V_2O_5 structure, the thickness of a single layer is determined to be about 0.24 nm and the interlayer spacing between monolayers is about 0.39 nm (Figure 2i), which is larger than the radius of Zn^{2+} (0.074 nm) and could provide the large space and abundant channels for efficient Zn^{2+} ions (de)intercalation.[34] All these observations strongly suggest the construction of the VOG composite through an ultrafast thermal shock treatment based on the FJH technique.

Figure S3 shows the X-ray diffraction (XRD) patterns of the as-resulted VOG composite, in which a series of sharp peaks are indexed to crystalline VO_2 (JCPDS No. 70-3131) and several weaker peaks are corresponded to V_2O_5 (JCPDS No. 89-0612) and carbon (JCPDS No. 41-1487) phases. Raman measurements have also unveiled the formation of the VOG composite. As shown in Figure S4, the characteristic peaks of V_2O_5 and VO_2 as well as the intense D (~1360 cm^{-1}) and G bands (~1587 cm^{-1}) for multilayer graphene are observed in the VOG composite.[35,36] Figure S5 presents the thermogravimetric analysis (TGA) curve of the VOG composite, which reveals that the approximate weight percentages of graphene-like carbon nanosheets, VO_2, and V_2O_5 in the VOG composite are 4.0, 48.23, and 47.23%, respectively. Furthermore, X-ray photoemission spectroscopy (XPS) and X-ray absorption spectroscopy (XAS) characterizations were conducted to explore the electronic structure and composition of the prepared VOG composite. As demonstrated in the XPS survey spectra in Figure S6, obvious V and O signals with a stronger C peak than that of the commercial V_2O_5 powder are detected in the VOG composite, accounting for the coexistence of vanadium oxides and graphene-like carbon nanosheets. The high-resolution V 2p XPS spectra in Figure 3a display two group peaks of V $2p_{1/2}$ and V $2p_{3/2}$, which reveals the presence of V^{3+}, V^{4+}, and V^{5+} (atomic ratios are about 1:4:2) from three fitting peaks in the VOG composite.[37] Figure 3b shows the C K-edge XAS spectra of the as-prepared VOG composite compared to that of the graphite paper substrate. At first glance, a lower intensity of the π^*C–C peak of the VOG composite than that of the graphite paper is observed, which as an indication of fewer sp^2-hybridized carbon atoms in the graphene reveals the incorporation of multilayered graphene in the VOG composite.[38] Furthermore, an additional peak at 288.7 eV deriving from the C–O–V bonds between VO_2–V_2O_5 and multilayered graphene is found in the C K-edge XAS of the VOG composite, manifesting the strong interactions of multilayered graphene-like carbon nanosheets and VO_2/V_2O_5 microstructure and it will be beneficial for the interfacial charge transfer.[39]

A coin cell was assembled for the electrochemical measurements using the as-prepared VOG composite as the cathode, the Zn foil as the anode, and 3 M $Zn(CF_3SO_3)_2$ aqueous solution as the electrolyte. Figure 4a shows the initial ten cyclic voltammetry (CV) curves of the VOG cathode at a scan rate of 0.1 mV s^{-1}. In the first anodic scan, two significant oxidation peaks located at ~1.54 and ~1.32 V vs Zn/Zn^{2+} are detected, and then, they gradually vanish in the following cycles. It is well documented that this phenomenon is strongly correlated with the decomposition of H_2O, resulting in a low Coulombic efficiency (CE).[40] In addition, it can be seen that the enclosed area of the CV curves of the VOG cathode drastically increased as the scan progressed. Generally, the enclosed area of the CV

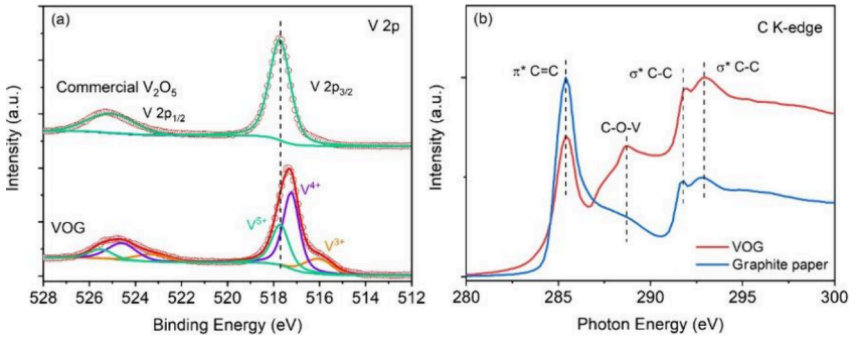

Figure 3. (a) High-resolution V 2p XPS spectra of the commercial V_2O_5 and VOG samples and (b) C K-edge XAS spectra of the commercial graphite paper and VOG samples.

https://doi.org/10.1021/acsami.4c10376
ACS Appl. Mater. Interfaces XXXX, XXX, XXX–XXX

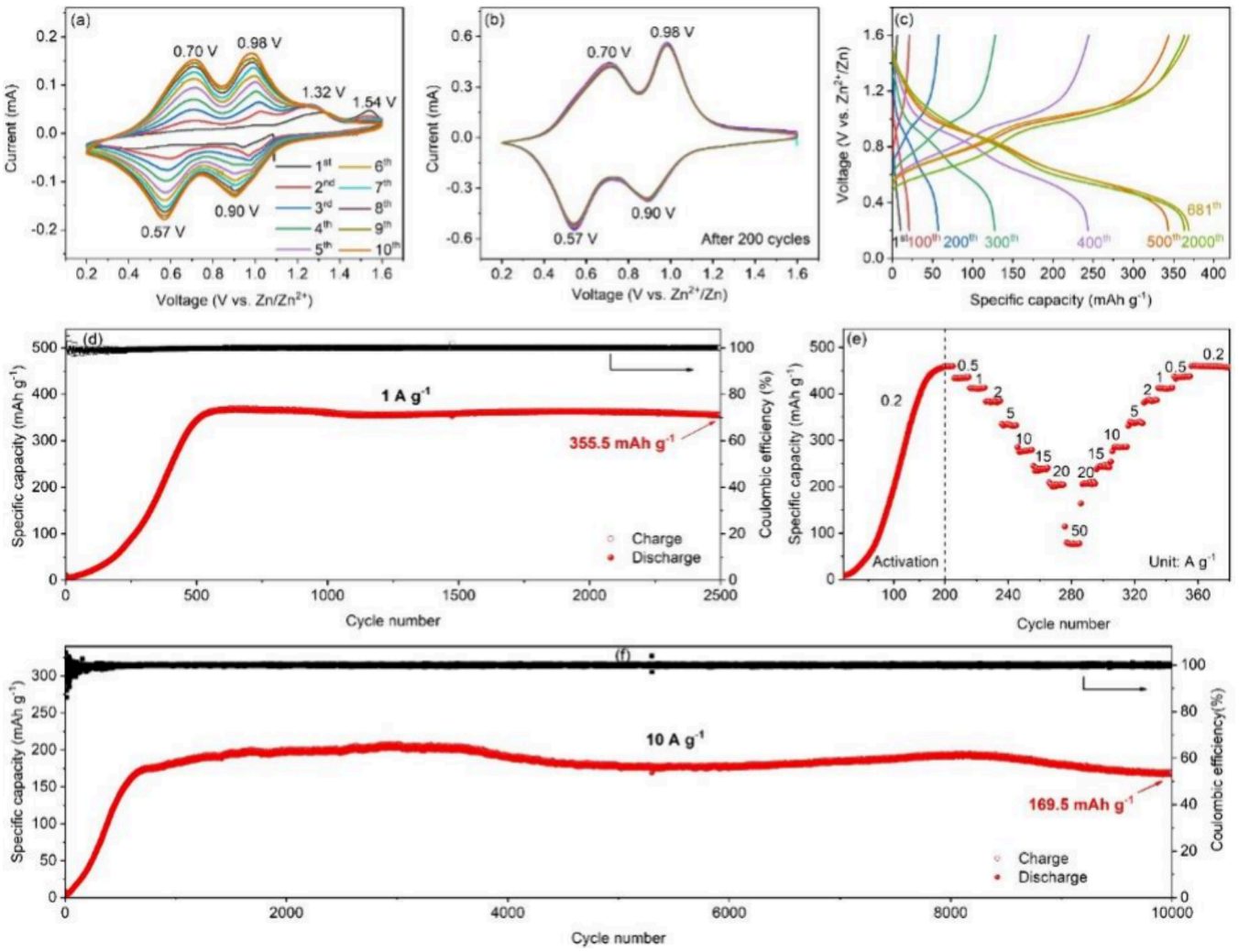

Figure 4. CV curves at the initial ten cycles (a) and at stabilization states after the activation (b), galvanostatic charge/discharge profiles (c), cycling performance at 1 A g^{-1} (d), rate performance at various currents ranging from 0.2 to 50 A g^{-1} (e), and long-term cycling performance at 10 A g^{-1} (f) of the VOG electrode.

profile is proportional to the capacity of the electrode at a certain scan rate, and thus, the increase of the enclosed area and the alters in the peak position of CV scans imply that there is a gradual activation process in the VOG cathode.[41] This finding is further evidenced by the electrochemical impedance spectroscopy (EIS) measurements in Figure S7, where a gradual decrease in the electrode resistance with the cycling is observed.[42] After the activation for the initial cycling (~200 cycles at 0.2 A g^{-1}), two groups of redox peaks with good symmetry at ~0.98/0.90 V and ~0.70/0.57 V are observed in the stabilized CV profiles (Figure 4b), corresponding to the multistep Zn^{2+} extraction/insertion and also demonstrating the good electrochemical reversibility of the VOG composite.[43,44]

Figure 4c,d presents the galvanostatic charge−discharge (GCD) profiles and cyclic performance of the VOG cathode at a low current density of 1 A g^{-1}, respectively. An obvious activation process of a gradually increased capacity from nearly zero in the first cycle to a maximum value of approximately 369 mA h g^{-1} at 681 cycles is found. This phenomenon is generally attributed to the increasing number of storage sites at the interface of cathode materials on repeated cycling, facilitated by the penetration of the electrolyte.[45] After the activation, a high discharge capacity of 355.5 mA h g^{-1} after 2500 cycles is maintained for the VOG cathode, while the commercial V_2O_5 electrode delivers a drastic decline in capacity after the activation (Figure S8), indicating the extraordinary structure stability of the VOG cathode. Figure 4e presents the rate performance of the VOG cathode at different current densities ranging from 0.2 to 50 A g^{-1}. After activation at 0.2 A g^{-1} for 200 cycles, the VOG cathode achieves remarkable discharge capacities of 459, 434, 412, 382, 334, 277, 236, 205, and 78 mA h g^{-1} at 0.2, 0.5, 1, 2, 5, 10, 15, 20, and 50 A g^{-1}, respectively. Upon the current density gradually switching from 50 A g^{-1} back to 0.2 A g^{-1}, the discharge capacity of the VOG cathode recovered from 78 mA h g^{-1} back to 459 mA h g^{-1}, implying high reversibility. In addition, the long-term cyclability of the VOG cathode was measured and optimized (Figure S9, where the optimal sintering temperature is 1100 °C) at high current densities of 10 A g^{-1}. As observed in Figure 4f, the optimal VOG cathode delivers a high initial discharge capacity of about 200 mA h g^{-1} after the activation and retains 169.5 mA h g^{-1} after 10,000 cycles, corresponding to a capacity retention of 85% (the capacity retention is calculated against the highest discharge capacity), which exceeds the performance of the commercial V_2O_5 cathode at the same current density (Figure S9). Table S1 demonstrates a comparison of the electro-

https://doi.org/10.1021/acsami.4c10376
ACS Appl. Mater. Interfaces XXXX, XXX, XXX−XXX

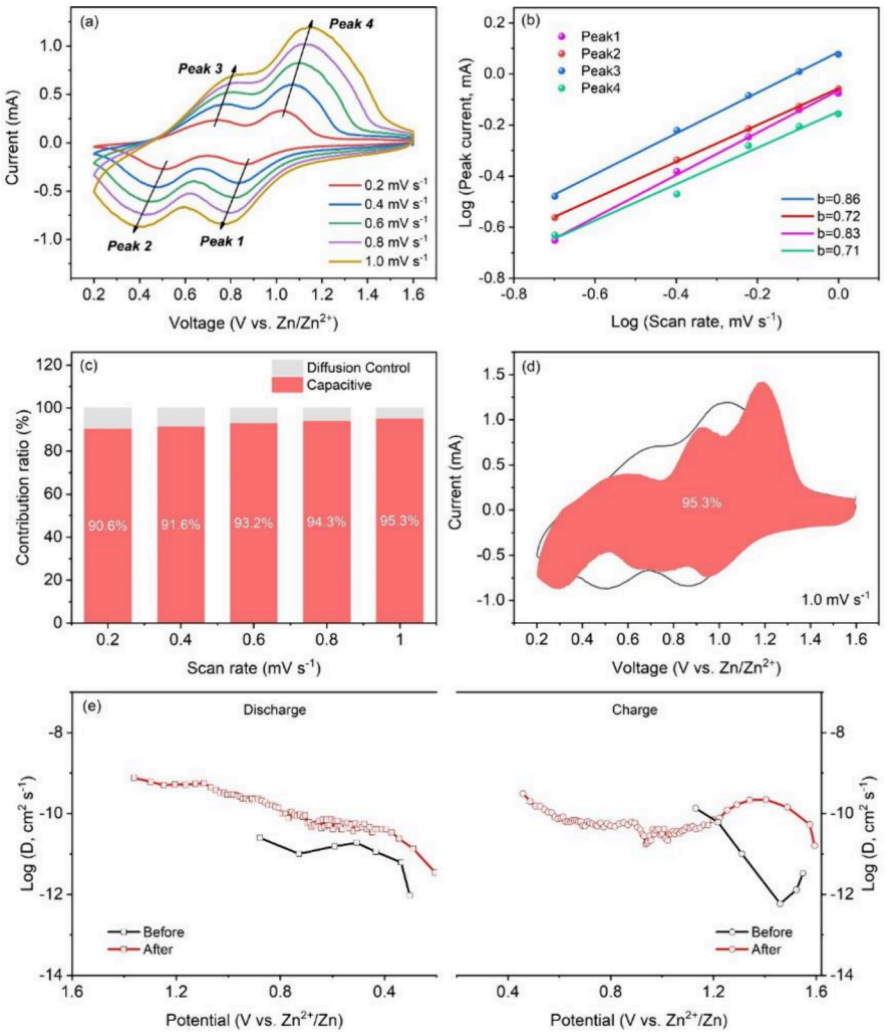

Figure 5. CV profiles of the VOG composite at varying scan rates from 0.2 to 1.0 mV s^{-1} (a), curves of log (i) vs log (ν) and the corresponding b values (b), contributions of diffusion- and capacity-controlled at different scan rates (c) and 1.0 mV s^{-1} (d), and Zn^{2+} diffusion coefficients of the VOG cathode before cycling and after the activation (stabilization) states based on GITT measurements (e).

chemical performance of the VOG cathode with other vanadium oxide cathodes in recent studies, where the competitive performance strongly suggests the high feasibility of the FJH technique in fabricating high-performance vanadium-based cathodes.

To understand the electrochemical kinetics of the VOG cathode, CV measurements (after the activation) at the sweep rate from 0.1 to 1 mV s^{-1} were performed, which can be utilized to determine the ratio of capacitive and diffusion contribution to the capacity.[46,47] As shown in Figure 5a, the relationship between the peak current (i) and the sweep rate (v) is described below:

$$i = av^b \tag{2}$$

where a and b are adjustable parameters, i is current, and v is the sweeping rate. When the b value is 1, it is a surface capacitance-controlled behavior, whereas the value of 0.5 means a diffusion-controlled behavior.[46,47] After the calculation, the b-values for peaks 1−4 of the VOG cathode are determined as 0.86, 0.72, 0.83, and 0.71, respectively (Figure 5b), indicating that the electrochemical reaction in the VOG cathode is mainly dominated by the capacitive behavior. Furthermore, the capacitance-controlled capacities (k_1v) and diffusion-controlled capacities ($k_2v^{1/2}$) can be quantitatively calculated by the following equation:

$$i = k_1v + k_2v^{1/2} \tag{3}$$

As presented in Figure 5c,d, the calculation results show that the ratio of capacitive contribution of the VOG cathode gradually increases with the increasing scan rate and it reaches as high as 95.3% at 1.0 mV s^{-1}, which indicates that the integration of graphene-like carbon nanosheets and the layer-stacked VO_2/V_2O_5 heterostructure induces the facilitated absorption kinetics of Zn^{2+} ions toward to the excellent rate performance. Additionally, galvanostatic intermittent titration technique (GITT) curves before the cycling and at the stabilization states after the activation were collected to further investigate the charge diffusion coefficient in the VOG cathode (Figure S10). As presented in Figure 5e (see detailed calculations in Supporting Information), the D_{Zn}^{2+} values during both the discharge and charge processes drastically increase after activating for 200 cycles at 0.2 A g^{-1}, indicating the faster Zn^{2+} diffusion for the increased electrochemical performance.[48]

To gain more insights into the performance enhancement of the VOG composite, the electrochemical active surface area

https://doi.org/10.1021/acsami.4c10376
ACS Appl. Mater. Interfaces XXXX, XXX, XXX−XXX

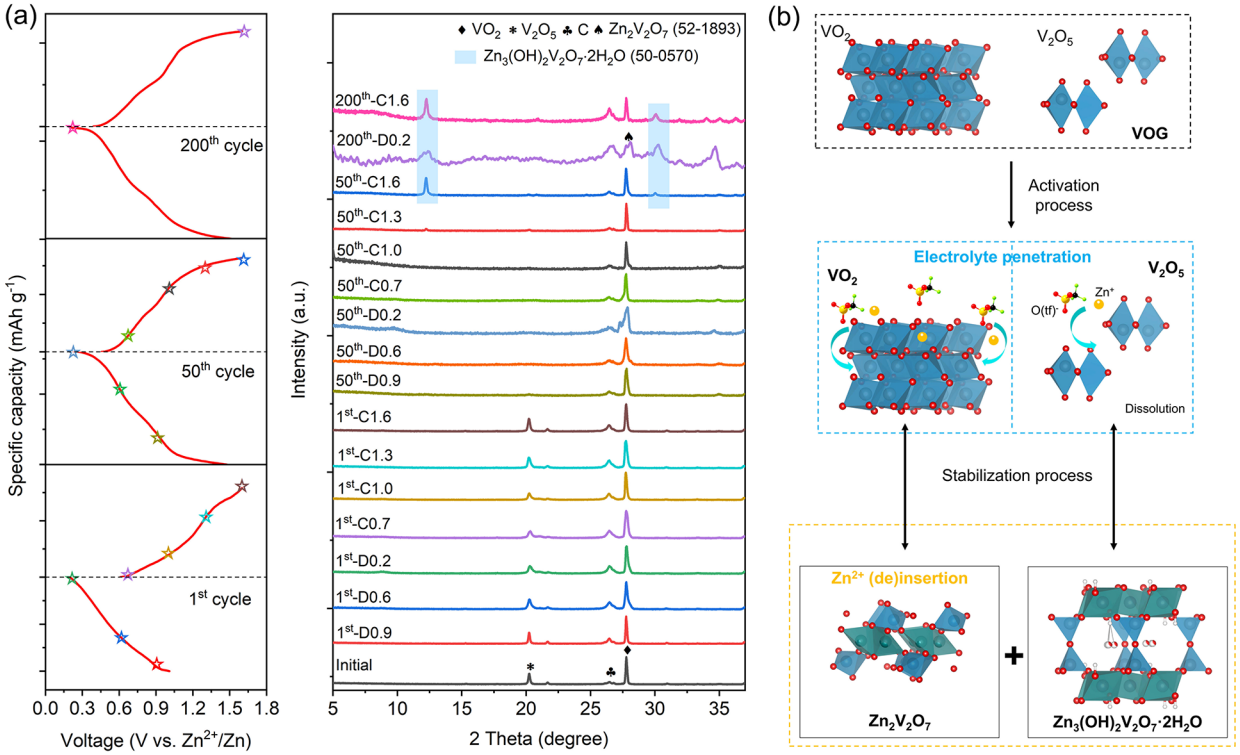

Figure 6. (a) Ex-situ XRD patterns of the VOG cathode at charge/discharge states in the activation (1st and 50th cycles) and stabilization processes (200th cycles) at 0.2 A g^{-1} and corresponding GCD curves. (b) Schematic illustration for the storage mechanism of the VOG cathode during activation and stabilization cycling processes.

(ECSA) of both the commercial V_2O_5 and VOG samples was investigated by measuring CV curves in non-Faradaic areas at various scan rates (Figure S11). Typically, the ECSA reflects the intrinsic storage sites of electrodes and is positively correlated with electrochemical double-layer capacitance (C_{dl}).[49] As illustrated in Figure S12, the C_{dl} values for the VOG composite before cycling and at stabilization states are 5.43 and 228.36 μF cm^{-2}, respectively. It suggests that the increased capacity of the VOG electrode during the activation process can be attributed to the growing number of storage sites owing to the gradual penetration of the electrolyte solution.[40,45,50] Moreover, these C_{dl} values for the VOG composite are notably higher than those of the commercial V_2O_5 sample (2.27 and 97.91 μF cm^{-2}, respectively), indicating that the VO_2/V_2O_5 heterostructure in the VOG electrode could greatly accelerate the ions adsorption/insertion process by providing extra storage sites.[49]

Additionally, it is well documented that the construction of heterostructure can not only offer extra storage sites to accelerate Zn^{2+} ions diffusion but also create the built-in electric field that facilitates charge transfer.[49,51] To verify this, the energy levels of commercial V_2O_5 and the VOG composite were measured using ultraviolet photoelectron spectroscopy (UPS). As displayed in Figure S13, the commercial V_2O_5 sample has a work function of approximately 5.13 eV, whereas the VOG composite exhibits a reduced work function of around 4.87 eV. Such difference in the work function would create a built-in electric field at the heterostructure interface to greatly facilitate the charge transfer and ions diffusion in the VOG composite, as confirmed by the higher Zn^{2+} diffusion coefficient in GITT curves (Figure S14) and the lower charge transfer resistance (R_{ct}) in EIS plots (Figure S15).

Based on the above analyses, the improved electrochemical performance of the VOG composite can be attributed to the following synergistic merits: (i) the high conductivity and large surface area of graphene-like carbon nanosheets significantly benefit charge transport and also buffer the volume expansion to maintain the architecture during cycling, as supported by SEM and HRTEM characterizations of the VOG composite cathode after cycling for 200 cycles (Figure S16); and (ii) the VO_2/V_2O_5 heterostructure not only provides extra storage sites but also generates a built-in electric field at the heterostructure interface, further promoting the charge transfer and Zn^{2+} ions diffusion. However, the micrometer scale of the layer-stacked VO_2/V_2O_5 heterostructure renders slower electrolyte penetration. Consequently, the abundant interfacial storage sites in the VO_2/V_2O_5 heterostructure are exposed and utilized gradually as cycling progresses, leading to an activation process during the initial cycles.

The ex-situ XRD characterizations are conducted to elucidate the storage mechanism of the VOG cathode from the view of structural evolution. As presented in Figure 6a, during the activation period (1st and 50th cycles), the diffraction peak of the V_2O_5 phase (located at 20.2°) gradually vanishes, which might be attributed to the vanadium dissolution caused by the H^+ intercalation from the dissociation of H_2O molecules.[52,53] As shown in Figure S17a, the indices of the diffraction peaks to the $H_{7.24}V_6O_{13}$ phase (JCPDS: 37-0172) are detected in the XRD pattern of the VOG composite at the full discharge state of the first cycle. Additionally, an obvious peak assigned to the O−H bond and a relatively weak peak related to the V−O bond are also observed in the O 1s XPS spectra at the full discharge state of the first cycle (Figure S17b), proving the insertion of H^+ ions.[54]

https://doi.org/10.1021/acsami.4c10376
ACS Appl. Mater. Interfaces XXXX, XXX, XXX−XXX

Moreover, ex-situ XRD patterns have revealed the formation of the $Zn_3(OH)_2V_2O_7{\cdot}2H_2O$ (ZVOH, JCPDS No. 50-0570) phase alongside the dissolution of V_2O_5 during the activation process, resulting from the reaction between Zn^{2+} ions, H_2O molecules and soluble vanadium ions ($VO_2(OH)^{2-}$) due to the dissolution of V_2O_5.[55] Previous studies have reported that the formation of the ZVOH phase during cycling could enhance the stability of vanadium-based cathodes due to its higher stability.[18,55] Therefore, benefiting from the transformation of V_2O_5 into ZVOH during the activation process, the VO_2 in the VOG composite remains with a reversible intermediate phase of $Zn_2V_2O_7$ (JCPDS No. 52-1893) emerging at the full discharge state and then disappearing at the charge states (Figure 6a). It indicates the reversible Zn^{2+} extraction/insertion into the host framework of VO_2 during stable cycling. Based on these findings, the storage mechanism of the VOG cathode can be described as follows: in the activation period, the VOG cathode undergoes the transformation of the V_2O_5 component into the ZVOH phase through vanadium dissolution and subsequent reaction with Zn^{2+} ions and water molecules, and concurrently the gradual penetration of electrolyte to provide more Zn^{2+} storage sites for the reversible Zn^{2+} insertion. Subsequently, in the stable period, the presence of the ZVOH phase and the reversible Zn^{2+} insertion in the VO_2 host contribute to stable capacity retention, as illustrated in Figure 6b and as below:

Activation process (vanadium dissolution with gradual electrolyte penetration):

$$V_2O_5 + H_2O \rightarrow H^+ + VO_2(OH)^{2-} \quad (4)$$

$$Zn^{2+} + VO_2(OH)^{2-} + H_2O \rightarrow Zn_3(OH)_2V_2O_7{\cdot}2H_2O + H^+ \quad (5)$$

$$VO_2 + Zn^{2+} + H^+ \rightarrow Zn_2V_2O_7 + H_{7.24}V_6O_{13} \quad (6)$$

Stable cycling process after the activation:
Discharge:

$$Zn^{2+} + VO_2 \rightarrow Zn_2V_2O_7 \quad (7)$$

Charge:

$$Zn_2V_2O_7 \rightarrow VO_2 + Zn^{2+} \quad (8)$$

CONCLUSIONS

In summary, we demonstrate a facile and ultrafast synthesis of a composite composed of layer-stacked VO_2/V_2O_5 microstructures and graphene-like carbon nanosheets via the FJH technique. As the cathode for aqueous ZIBs, the as-prepared composite achieves admirable stabilities of 355.5 mA h g^{-1} after 2500 cycles at 1.0 A g^{-1} and 169.5 mA h g^{-1} after 10,000 cycles at 10 A g^{-1}. Further electrochemical measurements reveal that the comparable performance could be attributed to the accelerated electron/Zn^{2+} transfer and the alleviated structure degradation benefitted from abundant sites and a built-in electric field of the layer-stacked VO_2/V_2O_5 heterostructure, as well as the excellent electric conductivity of graphene-like carbon nanosheets. This work may provide a novel and efficient approach for obtaining high-performance vanadium oxide-based cathodes toward efficient ZIBs.

METHODS

Sample Preparation. For the synthesis of the VOG composite, 500 mg of the commercial V_2O_5 powder (99.99%, Rhawn, Shanghai, China) was evenly placed on the graphite paper (length: 10 cm, width: 0.8 cm, thickness: 0.3 mm; Beijing Jinglong Special Carbon Co. Ltd.) and then it was sealed in a quartz tube with ceramic plugs. Afterward, the ends of the graphite paper were connected with the copper contacts of the FJH equipment (Hefei In-situ High-tech Co., Ltd.), as demonstrated in Figure S1. Finally, after an ultrafast heating/quenching treatment (quick mode, input voltage: 15 V, input current: 150 A, heating temperature: ~1100 °C), the VOG composite was obtained. For optimization, samples treated at 800 °C (VOG-800) and 1400 °C (VOG-1400) were prepared by adjusting the input electric voltage and current to 10 V and 100 A for VOG-800, and 20 V and 150 A for VOG-1400, respectively.

Structural Characterization. Scanning electron microscopy (SEM, Quanta FEG 250, FEI) and high-resolution transmission electron microscopy (HRTEM, JEOL 2100F, 200 keV) equipped with energy-dispersive X-ray spectroscopy (EDX, Oxford Instruments Inc.) were employed to investigate the morphologies of as-synthesized samples. The crystal structure was explored by X-ray diffraction (XRD) with a copper (Cu) Kα source (Shimadzu XRD-6000). The chemical structure and component were analyzed by X-ray photoelectron spectroscopy (XPS, Thermo Scientific K-Alpha) and X-ray absorption spectroscopy (XAS, Beijing Synchrotron Radiation Facility (Beamline 4B9B)) characterizations. Raman spectra were collected by RTS-II, Zolix. TGA was explored by a TA SDT Q600 in the air from room temperature to 1000 °C with a heating rate of 10 °C min^{-1}.

Electrochemical Measurements. The electrochemical performance was evaluated using a CR2025 coin-type cell that was assembled in an air atmosphere and consisted of the working electrodes (cathode), Zn foil (anode), separator (glass fiber, Whatman GF/D), and electrolyte (3 M $Zn(CF_3SO_3)_2$). The working electrodes were prepared by pasting a slurry that mixed as-obtained samples, acetylene black, and poly(vinylidene fluoride, PVDF) with a weight ratio of 7:2:1 in *N*-methylpyrrolidone (NMP) onto the titanium foil and drying at 80 °C overnight in a vacuum oven. The galvanostatic discharge−charge measurements at various current densities from 0.2 to 10 A g^{-1} in the voltage range 0.2−1.6 V were carried out on LAND CT3001A battery test systems. Cyclic voltammetry (CV) and electrochemical impedance spectroscopy (EIS) from 100 kHz to 10 mHz of as-fabricated electrodes were performed using an electrochemical workstation (Ivium Vertex.C).

ASSOCIATED CONTENT

Supporting Information

The Supporting Information is available free of charge at https://pubs.acs.org/doi/10.1021/acsami.4c10376.

Photographs of the experimental setup, XRD patterns, Raman spectra, XPS spectra, cycling performance, GITT plots, and the calculation method of Zn^{2+} diffusion coefficient (PDF)

AUTHOR INFORMATION

Corresponding Authors

Jiujun Deng − *Automotive Engineering Research Institute, Institute for Energy Research, Jiangsu University, Zhenjiang 212013, China;* orcid.org/0000-0002-1740-0786; Email: jjDeng@ujs.edu.cn

Xuhui Sun − *Institute of Functional Nano and Soft Materials Laboratory (FUNSOM), Jiangsu Key Laboratory of Advanced Negative Carbon Technologies, Soochow University, Suzhou 215123, China;* orcid.org/0000-0003-0002-1146; Email: xhsun@suda.edu.cn

https://doi.org/10.1021/acsami.4c10376
ACS Appl. Mater. Interfaces XXXX, XXX, XXX−XXX

Authors

Xiaoxin Lv − *Automotive Engineering Research Institute, Institute for Energy Research, Jiangsu University, Zhenjiang 212013, China*

Aomen Yang − *Automotive Engineering Research Institute, Institute for Energy Research, Jiangsu University, Zhenjiang 212013, China*

Menglian Wang − *Automotive Engineering Research Institute, Institute for Energy Research, Jiangsu University, Zhenjiang 212013, China*

Kaiqi Nie − *Institute of High Energy Physics, Chinese Academy of Sciences, Beijing 100049, China*

Complete contact information is available at: https://pubs.acs.org/10.1021/acsami.4c10376

Author Contributions

All authors have given approval to the final version of the manuscript.

Notes

The authors declare no competing financial interest.

■ ACKNOWLEDGMENTS

We acknowledge the financial support from Jiangsu Key Laboratory of Advanced Negative Carbon Technologies and Jiangsu Key Laboratory for Carbon-Based Functional Materials and Devices, Soochow University (KJS2206) and National Natural Science Foundation of China (51902139). This work is also supported by Collaborative Innovation Center of Suzhou Nano Science and Technology, the Priority Academic Program Development of Jiangsu Higher Education Institutions (PAPD), the 111 Project, Suzhou Key Laboratory of Functional Nano and Soft Materials, and Soochow University-Western University Centre for Synchrotron Radiation Research.

■ REFERENCES

(1) Zhu, Z.; Jiang, T.; Ali, M.; Meng, Y.; Jin, Y.; Cui, Y.; Chen, W. Rechargeable Batteries for Grid Scale Energy Storage. *Chem. Rev.* **2022**, *122*, 16610−16751.

(2) Guo, Z.; Qian, G.; Wang, C.; Zhang, G.; Yin, R.; Liu, W.-D.; Liu, R.; Chen, Y. Progress in Electrode Materials for the Industrialization of Sodium-Ion Batteries. *Prog. Nat. Sci.: Mater. Int.* **2023**, *33*, 1−7.

(3) Song, Z.; Liu, R.; Liu, W.; Chen, Y.; Hu, W. Low-Cost Polyanion-Type Cathode Materials for Sodium-Ion Battery. *Adv. Energy Sustainability Res.* **2023**, *4*, No. 2300102.

(4) Li, G.; Li, T.; Jiang, M.; Somoro, R. A.; Sun, N.; Xu, B. Self-Propagating Fabrication of a 3D Graphite@rGO Film Anode for High-performance Potassium-Ion Batteries. *ACS Appl. Mater. Interfaces* **2024**, *16*, 42118−42127.

(5) Zhang, N.; Chen, X.; Yu, M.; Niu, Z.; Cheng, F.; Chen, J. Materials Chemistry for Rechargeable Zinc-Ion Batteries. *Chem. Soc. Rev.* **2020**, *49*, 4203−4219.

(6) Liu, S.; Zhang, R.; Wang, C.; Mao, J.; Chao, D.; Zhang, C.; Zhang, S.; Guo, Z. Zinc Ion Batteries: Bridging the Gap from Academia to Industry for Grid-Scale Energy Storage. *Angew. Chem., Int. Ed.* **2024**, *63*, No. e202400045.

(7) Ge, H.; Qin, L.; Zhang, B.; Jiang, L.; Tang, Y.; Lu, B.; Tian, S.; Zhou, J. An Ionically Cross-Linked Composite Hydrogel Electrolyte Based on Natural Biomacromolecules for Sustainable Zinc-Ion Batteries. *Nanoscale Horiz.* **2024**, *9*, 1514−1521.

(8) Li, J.; Liu, Z.; Han, S.; Zhou, P.; Lu, B.; Zhou, J.; Zeng, Z.; Chen, Z.; Zhou, J. Hetero Nucleus Growth Stabilizing Zinc Anode for High-Biosecurity Zinc-Ion Batteries. *Nano-Micro Lett.* **2023**, *15*, 237.

(9) Wang, X.; Zhang, Z.; Xi, B.; Chen, W.; Jia, Y.; Feng, J.; Xiong, S. Advances and Perspectives of Cathode Storage Chemistry in Aqueous Zinc-Ion Batteries. *ACS Nano* **2021**, *15*, 9244−9272.

(10) Wan, F.; Liu, R.; Xia, Y.; Hu, K.; Lei, Y.; Wang, C.; Zhang, S.; Li, S.; Yang, D.; Zheng, Y.; Chen, W. Phase-Modified Strongly Coupled δ/ε-MnO_2 Homojunction Cathode for Kinetics-Enhanced Zinc-Ion Batteries. *Inorg. Chem.* **2024**, *63*, 6988−6997.

(11) Du, G.; Pang, H. Recent Advancements in Prussian Blue Analogues: Preparation and Application in Batteries. *Energy Storage Mater.* **2021**, *36*, 387−408.

(12) Peng, Z.; Feng, Z.; Zhou, X.; Li, S.; Yin, X.; Zhang, Z.; Zhao, N.; He, Z.; Dai, L.; Wang, L.; Lu, C. Polymer Engineering for Electrodes of Aqueous Zinc Ion Batteries. *J. Energy Chem.* **2024**, *91*, 345−369.

(13) Liu, H.; Jiang, L.; Cao, B.; Du, H.; Lu, H.; Ma, Y.; Wang, H.; Guo, H.; Huang, Q.; Xu, B.; Guo, S. Van der Waals Interaction-Driven Self-Assembly of V_2O_5 Nanoplates and MXene for High-Performing Zinc-Ion Batteries by Suppressing Vanadium Dissolution. *ACS Nano* **2022**, *16*, 14539−14548.

(14) Lv, T.; Peng, Y.; Zhang, G.; Jiang, S.; Yang, Z.; Yang, S.; Pang, H. How About Vanadium-Based Compounds as Cathode Materials for Aqueous Zinc Ion Batteries? *Adv. Sci.* **2023**, *10*, No. 2206907.

(15) Zhou, T.; Xie, L.; Han, Q.; Qiu, X.; Xiao, Y.; Yang, X.; Liu, X.; Yang, S.; Zhu, L.; Cao, X. Progress and Prospect of Vanadates as Aqueous Zn-Ion Batteries Cathodes. *Coord. Chem. Rev.* **2024**, *498*, No. 215461.

(16) Zhu, K.; Wei, S.; Shou, H.; Shen, F.; Chen, S.; Zhang, P.; Wang, C.; Cao, Y.; Guo, X.; Luo, M.; Zhang, H.; Ye, B.; Wu, X.; He, L.; Song, L. Defect Engineering on V_2O_3 Cathode for Long-Cycling Aqueous Zinc Metal Batteries. *Nat. Commun.* **2021**, *12*, 6878.

(17) Liu, Y.; Wang, T.; Sun, Y.; Zhang, M.; Gao, G.; Yang, J.; Cai, K. Fast and Efficient In-Situ Construction of Low Crystalline PEDOT-Intercalated V_2O_5 Nanosheets for High-Performance Zinc-Ion Battery. *Chem. Eng. J.* **2024**, *484*, No. 149501.

(18) Lu, Y.; Zhu, T.; van den Bergh, W.; Stefik, M.; Huang, K. A High Performing Zn-Ion Battery Cathode Enabled by In Situ Transformation of V_2O_5 Atomic Layers. *Angew. Chem., Int. Ed.* **2020**, *59*, 17004.

(19) He, Q.; Wang, H.; Bai, J.; Liao, Y.; Wang, S.; Chen, L. Bilayered Nanostructured V_2O_5 nH_2O Xerogel Constructed 2D Nano-Papers for Efficient Aqueous Zinc/Magnesium Ion Storage. *J. Colloid Interface Sci.* **2024**, *662*, 490−504.

(20) Muthukumar, K.; Rajendran, S.; Sekar, A.; Chen, Y.; Li, J. Synthesis of V_2O_5 Nanoribbon-Reduced Graphene Oxide Hybrids as Stable Aqueous Zinc-Ion Battery Cathodes via Divalent Transition Metal Cation-Mediated Coprecipitation. *ACS Sustainable Chem. Eng.* **2023**, *11*, 2670−2679.

(21) Wang, M.; Nie, K.; Wu, H.; Lv, X.; Deng, J.; Ji, H. Carbon Nanotubes Intertwined Porous Vanadium Oxide Heterostructured Microfibers as High-Performance Cathodes for Aqueous Zinc-Ion Batteries. *Appl. Surf. Sci.* **2023**, *612*, No. 155791.

(22) Hong, J.; Xie, L.; Shi, C.; Lu, X.; Shi, X.; Cai, J.; Wu, Y.; Shao, L.; Sun, Z. High-Performance Aqueous Zinc-Ion Batteries Based on Multidimensional V_2O_3 Nanosheets@Single-Walled Carbon Nanohorns@Reduced Graphene Oxide Composite and Optimized Electrolyte. *Small Methods* **2023**, *20*, No. 2300205.

(23) Li, X.; Chen, F.; Zhao, B.; Zhang, S.; Zheng, X.; Wang, Y.; Jin, X.; Dai, C.; Wang, J.; Xie, J.; Zhang, Z.; Zhao, Y. Ultrafast Synthesis of Metal-Layered Hydroxides in a Dozen Seconds for High-Performance Aqueous Zn (Micro-) Battery. *Nano-Micro Lett.* **2023**, *15*, 32.

(24) Wyss, K. M.; Luong, D. X.; Tour, J. M. Large-Scale Syntheses of 2D Materials: Flash Joule Heating and Other Methods. *Adv. Mater.* **2022**, *34*, No. 2106970.

(25) Lai, L.; Li, J.; Deng, Y.; Yu, Z.; Wei, L.; Chen, Y. Carbon and Carbon/Metal Hybrid Structures Enabled by Ultrafast Heating Methods. *Small Struct.* **2022**, *3*, No. 2200112.

(26) Li, G.; Zhang, W.; Nie, K.; Lv, X.; Deng, J.; Ji, H. Flash Joule Heating to Enhance Water Oxidation of Hematite Photoanode via

Mediating with An Oxidized Carbon Overlayer. *Carbon* **2023**, *215*, No. 118444.
(27) Luong, D. X.; Bets, K. V.; Algozeeb, W. A.; Stanford, M. G.; Kittrell, C.; Chen, W.; Salvatierra, R. V.; Ren, M.; McHugh, E. A.; Advincula, P. A.; Wang, Z.; Bhatt, M.; Guo, H.; Mancevski, V.; Shahsavari, R.; Yakobson, B. I.; Tour, J. M. Gram-Scale Bottom-Up Flash Graphene Synthesis. *Nature* **2020**, *577*, 647.
(28) Xing, L.; Liu, R.; Gong, Z.; Liu, J.; Liu, J.; Gong, H.; Huang, K.; Fei, H. Ultrafast Joule Heating Synthesis of Hierarchically Porous Graphene-Based Co-N-C Single-Atom Monoliths. *Nano Res.* **2022**, *15*, 3913.
(29) Chen, Y.; Egan, G. C.; Wan, J.; Zhu, S.; Jacob, R. J.; Zhou, W.; Dai, J.; Wang, Y.; Danner, V. A.; Yao, Y.; Fu, K.; Wang, Y.; Bao, W.; Li, T.; Zachariah, M. R.; Hu, L. Ultra-Fast Self-Assembly and Stabilization of Reactive Nanoparticles in Reduced Graphene Oxide Films. *Nat. Commun.* **2016**, *7*, 12332.
(30) Zeng, C.; Duan, C.; Guo, Z.; Liu, Z.; Dou, S.; Yuan, Q.; Liu, P.; Zhang, J.; Luo, J.; Liu, W.; Zhang, J.; Chen, Y.; Hu, W. Ultrafastly Activated Needle Coke as Electrode Material for Supercapacitors. *Prog. Nat. Sci.: Mater. Int.* **2022**, *32*, 786−792.
(31) Yue, Y.; Liang, H. Micro- and Nano-Structured Vanadium Pentoxide (V_2O_5) for Electrodes of Lithium-Ion Batteries. *Adv. Energy Mater.* **2017**, *7*, No. 1602545.
(32) Fu, M.; Jiao, Q.; Zhao, Y. Preparation of $NiFe_2O_4$ Nanorod-Graphene Composites via An Ionic Liquid Assisted One-Step Hydrothermal Approach and Their Microwave Absorbing Properties. *J. Mater. Chem. A* **2013**, *1*, 5577−5586.
(33) Yan, Y.; Yin, Y.-X.; Guo, Y.-G.; Wan, L.-J. A Sandwich-Like Hierarchically Porous Carbon/Graphene Composite as a High-Performance Anode Material for Sodium-Ion Batteries. *Adv. Energy Mater.* **2014**, *4*, No. 1301584.
(34) Wang, C.; Chen, S.; Xie, H.; Wei, S.; Wu, C.; Song, L. Atomic Sn^{4+} Decorated into Vanadium Carbide MXene Interlayers for Superior Lithium Storage. *Adv. Energy Mater.* **2019**, *9*, No. 1802977.
(35) Shao, Z.; Cao, X.; Zhang, Q.; Long, S.; Chang, T.; Xu, F.; Yang, Y.; Jin, P. Fully Automatic Modulation for Broadband Sunlight Based on YO_xH_y/VO_2 Hybrid Structures. *Sol. Energy Mater. Sol. Cells* **2019**, *200*, No. 110044.
(36) Ivanov, A. V.; Maksimova, N. V.; Manylov, M. S.; Kirichenko, A. N.; Kalachev, I. L.; Malakho, A. P.; Avdeev, V. V. Gas Permeability of Graphite Foil Prepared from Exfoliated Graphite with Different Microstructures. *J. Mater. Sci.* **2021**, *56*, 4197−4211.
(37) Bi, W.; Deng, S.; Tang, H.; Liu, Y.; Shen, J.; Gao, G.; Wu, G.; Atif, M.; AlSalhi, M. S.; Cao, G. Coherent V^{4+}-Rich V_2O_5/Carbon Aerogel Nanocomposites for High Performance Supercapacitors. *Sci. China Mater.* **2022**, *65*, 1797−1804.
(38) Sharma, A.; Varshney, M.; Nanda, S. S.; Shin, H. J.; Kim, N.; Yi, D. K.; Chae, K.-H.; Won, S. O. Structural, Electronic Structure and Antibacterial Properties of Graphene-Oxide Nano-Sheets. *Chem. Phys. Lett.* **2018**, *698*, 85.
(39) Liu, Z.; Wang, M.; Liu, S.; Chen, Z.; Yang, L.; Sun, K.; Chen, Y.; Zeng, L.; Wang, W.; Zhao, J.; Sun, G.; Liu, B.; Pan, Y.; Liu, Y.; Liu, C. Design of Assembled Composite of Mn_3O_4@Graphitic Carbon Porous Nano-Dandelions: A Catalyst for Low-Temperature Selective Catalytic Reduction of NO_x with Remarkable SO_2 Resistance. *Appl. Catal., B* **2020**, *269*, No. 118731.
(40) Liu, Y.; Zou, Y.; Guo, M.; Hui, Z.; Zhao, L. Boosting the Active Sites and Kinetics of VO_2 by Mn Pre-Intercalated and PVP Modified Nanostructure to Improve the Cycle Stability for Aqueous Zinc Batteries. *Chem. Eng. J.* **2022**, *433*, No. 133528.
(41) Qin, H.; Yang, Z.; Chen, L.; Chen, X.; Wang, L. A High-Rate Aqueous Rechargeable Zinc Ion Battery Based on the VS_4@rGO Nanocomposite. *J. Mater. Chem. A* **2018**, *6*, 23757−23765.
(42) Zhang, N.; Dong, Y.; Jia, M.; Bian, X.; Wang, Y.; Qiu, M.; Xu, J.; Liu, Y.; Jiao, L.; Cheng, F. Rechargeable Aqueous Zn-V_2O_5 Battery with High Energy Density and Long Cycle Life. *ACS Energy Lett.* **2018**, *3*, 1366−1372.
(43) Yang, Y.; Tang, Y.; Fang, G.; Shan, L.; Guo, J.; Zhang, W.; Wang, C.; Wang, L.; Zhou, J.; Liang, S. Li^+ Intercalated $V_2O_5{\cdot}nH_2O$ with Enlarged Layer Spacing and Fast Ion Diffusion as An Aqueous Zinc-Ion Battery Cathode. *Energy Environ. Sci.* **2018**, *11*, 3157−3162.
(44) He, P.; Yan, M.; Liao, X.; Luo, Y.; Mai, L.; Nan, C.-W. Reversible V^{3+}/V^{5+} Double Redox in Lithium Vanadium Oxide Cathode for Zinc Storage. *Energy Storage Mater.* **2020**, *29*, 113−120.
(45) Soundharrajan, V.; Sambandam, B.; Kim, S.; Alfaruqi, M. H.; Putro, D. Y.; Jo, J.; Kim, S.; Mathew, V.; Sun, Y.-K.; Kim, J. $Na_2V_6O_{16}{\cdot}3H_2O$ Barnesite Nanorod: An Open Door to Display a Stable and High Energy for Aqueous Rechargeable Zn-Ion Batteries as Cathodes. *Nano Lett.* **2018**, *18*, 2402−2410.
(46) Wu, Z.; Yao, J.; Chen, C.; Chen, X.; Pan, X.; Zheng, J.; Gan, Y.; Li, J.; Liu, X.; Xia, C.; Lv, L.; Wang, H.; Wan, H. Ammonium Intercalation Engineering Regulated Structural Stability of V_6O_{13} Cathodes for Durable Zinc Ion Batteries. *Chem. Eng. J.* **2024**, *479*, No. 147889.
(47) Hu, H.; Zhao, P.; Li, X.; Liu, J.; Liu, H.; Sun, B.; Pan, K.; Song, K.; Cheng, H. Heterojunction Tunnelled Vanadium-Based Cathode Materials for High-Performance Aqueous Zinc Ion Batteries. *J. Colloid Interface Sci.* **2024**, *665*, 564−572.
(48) Li, R.; Zhang, H.; Zheng, Q.; Li, X. Porous V_2O_5 Yolk-Shell Microspheres for Zinc Ion Battery Cathodes: Activation Responsible for Enhanced Capacity and Rate Performance. *J. Mater. Chem. A* **2020**, *8*, 5186−5193.
(49) Deng, X.; Zhang, P.; Wan, Z.; Ma, Z.; Wang, X. Heterostructure Engineering of NiCo-LDHs for Enhanced Energy Storage Performance in Aqueous Zinc-Ion Batteries. *Small* **2024**, *20*, No. 2311332.
(50) Li, Z.; Wu, B.; Yan, M.; He, L.; Xu, L.; Zhang, G.; Xiong, T.; Luo, W.; Mai, L. Novel Charging-Optimized Cathode for a Fast and High-Capacity Zinc-Ion Battery. *ACS Appl. Mater. Interfaces* **2020**, *12*, 10420−10427.
(51) Chen, J.; Xiao, B.; Hu, C.; Chen, H.; Huang, J.; Yan, D.; Peng, S. Construction Strategy of VO_2@V_2C 1D/2D Heterostructure and Improvement of Zinc-Ion Diffusion Ability in VO_2 (B). *ACS Appl. Mater. Interfaces* **2022**, *14*, 28760−28768.
(52) Dai, Y.; Zhang, C.; Li, J.; Gao, X.; Hu, P.; Ye, C.; He, H.; Zhu, J.; Zhang, W.; Chen, R.; Zong, W.; Guo, F.; Parkin, I. P.; Brett, D. J. L.; Shearing, P. R.; Mai, L.; He, G. Inhibition of Vanadium Cathodes Dissolution in Aqueous Zn-Ion Batteries. *Adv. Mater.* **2024**, *36*, No. 2310645.
(53) Dou, X.; Xie, X.; Liang, S.; Fang, G. Low-Current-Density Stability of Vanadium-Based Cathodes for Aqueous Zinc-Ion Batteries. *Sci. Bull.* **2024**, *69*, 833−845.
(54) Qian, Y.; Wang, H.; Li, X.; Song, T.; Pei, Y.; Liu, L.; Long, B.; Wu, X.; Wang, X. Sn-Doped BiOCl Nanosheet with Synergistic H^+/Zn^{2+} Co-Insertion for "Rocking Chair" Zinc-Ion Battery. *J. Energy Chem.* **2023**, *81*, 623−632.
(55) Li, W.; Jiang, W.; Zhu, K.; Wang, Z.; Xie, W.; Yang, H.; Ma, M.; Yang, W. Unlocking the Performance Degradation of Vanadium-Based Cathodes in Aqueous Zinc-Ion Batteries. *Chem. Eng. J.* **2024**, *496*, No. 153786.

https://doi.org/10.1021/acsami.4c10376
ACS Appl. Mater. Interfaces XXXX, XXX, XXX−XXX